

# Residual Degradation Learning Unfolding Framework with Mixing Priors across Spectral and Spatial for Compressive Spectral Imaging

Yubo Dong Dahua Gao\* Tian Qiu Yuyan Li Minxi Yang Guangming Shi  
School of Artificial Intelligence, Xidian University

## Abstract

To acquire a snapshot spectral image, coded aperture snapshot spectral imaging (CASSI) is proposed. A core problem of the CASSI system is to recover the reliable and fine underlying 3D spectral cube from the 2D measurement. By alternately solving a data subproblem and a prior subproblem, deep unfolding methods achieve good performance. However, in the data subproblem, the used sensing matrix is ill-suited for the real degradation process due to the device errors caused by phase aberration, distortion; in the prior subproblem, it is important to design a suitable model to jointly exploit both spatial and spectral priors. In this paper, we propose a Residual Degradation Learning Unfolding Framework (RDLUF), which bridges the gap between the sensing matrix and the degradation process. Moreover, a Mix $S^2$  Transformer is designed via mixing priors across spectral and spatial to strengthen the spectral-spatial representation capability. Finally, plugging the Mix $S^2$  Transformer into the RDLUF leads to an end-to-end trainable and interpretable neural network RDLUF-Mix $S^2$ . Experimental results establish the superior performance of the proposed method over existing ones.

## 1. Introduction

To acquire a snapshot spectral image, coded aperture snapshot spectral imaging (CASSI) is proposed [1, 27, 36, 40], which utilizing a coded aperture and one or more dispersive elements to modulate a spectral scene. A sensor array captures a multiplexed 2D projection of the 3D data cube representing the scene. Therefore, a core problem of the CASSI system is to recover the reliable and fine underlying 3D hyperspectral image (HSI) cube from the 2D measurement.

Based on CASSI, a large number of reconstruction algorithms have been proposed to recover the 3D HSI cube from the 2D measurement, including model-based methods [18, 21, 22, 36, 39, 41, 44, 49], end-to-end methods [6, 15, 20, 27, 28], and deep unfolding methods [16, 37, 38]. Among them, deep unfolding methods achieves the most impressive performance without loss interpretability, as they convert conventional iterative optimization algorithms to a stack of

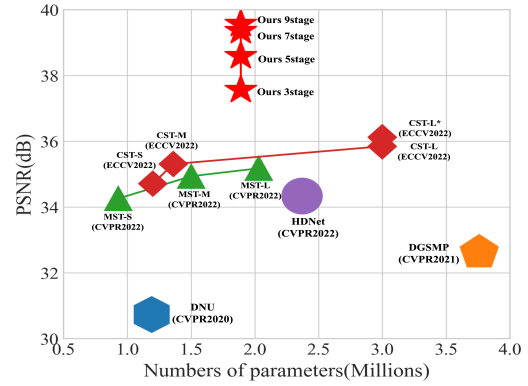


Figure 1. PSNR-Parameters comparisons with previous HSI reconstruction methods. The vertical axis is PSNR (in dB performance), and the horizontal axis is Parameters(memory cost). Our proposed Residual Degradation Learning Unfolding Framework with Mixing priors across Spatial and Spectral(RDLUF-Mix $S^2$ ) Transformers outperforms previous methods while requiring fewer parameters.

recurrent deep neural network (DNN) blocks. Often, deep unfolding methods alternately solve a data subproblem and a prior subproblem.

The data subproblem is highly related to the degradation process. The ways to acquire the degradation matrix in the data subproblem can be classified into two types, the first directly uses the sensing matrix as the degradation matrix [24, 26, 38] and the other learns the degradation matrix using a neural network [16, 29, 50]. However, since the sensing matrix is obtained from the equidistant lasers of different wavelengths on the sensor, it cannot reflect the device errors caused by phase aberration, distortion and alignment of the continuous spectrum. Thus, the earlier kind does not take into account the gap between the sensing matrix and the degradation process. In the latter type, directly modeling the degradation process is challenging. It is easier to optimize the residual mapping than to optimize the original, unreferenced mapping. Therefore, we explicitly model the degradation process as residual learning with reference to the sensing matrix.

The prior subproblem utilizes a trained denoiser to implicitly express the regularization term as a denoising

problem, which usually is an end-to-end neural network. Recently, the Spectral-wise Multi-head Self-Attention(S-MSA) is proposed to model long-range dependency, which calculates the self-attention with dependency on the spectral dimension. However, S-MSA models dependency on spectral dimension may sacrifice some useful spatial information of textures and structures, which is important for reproducing high quality HSI images. Thanks to the inductive bias, CNN excels the modeling ability of local similarity. Therefore, we introduce a multiscale convolution branch to strengthen the spatial modeling ability of S-MSA. The visual information is processed at various scales and then aggregated so that the next layer can abstract features from different scales simultaneously and hence capture more textures and details.

In this paper, we firstly unfold the Proximal Gradient Descent (PGD) algorithm based on maximum a posteriori (MAP) theory for HSI reconstruction. Then, we integrate the residual degradation learning strategy into the data subproblem of PGD, which bridges the gap between the sensing matrix and the degradation process, leading to our Residual Degradation Learning Unfolding Framework(RDLUF). Secondly, a multiscale convolution called Lightweight Inception is combined with the spectral self-attention in a parallel design to address the problem of weak spatial modeling ability of S-MSA. To provide complementary clues in the spectral and spatial branches, we propose bi-directional interactions across branches, which enhance the modeling ability in spectral and spatial dimensions respectively, resulting in our Mixing priors across Spatial and Spectral (Mix $S^2$ ) Transformer. Finally, plugging the Mix $S^2$  Transformer into the RDLUF as the denoiser of the prior subproblem leads to an end-to-end trainable and interpretable neural network RDLUF-Mix $S^2$ . Equipped with the proposed techniques, RDLUF-Mix $S^2$  with 9stage dramatically outperforms state-of-the-art (SOTA) HSI restoration methods by over 3.45 dB, as shown in Fig. 1.

In summaries, this work contributes as follows:

1. We propose an unfolding framework RDLUF, which bridge the gap between the sensing matrix and the degradation process.
2. We propose a spectral self-attention and convolution parallel structure, which enhances the spatial modeling capabilities of S-MSA.
3. We propose bi-directional interactions across branches, which improves the spectral-spatial representation capability by mixing prior across spatial and spectral, resulting in our Mix $S^2$  Transformer.

## 2. Related Work

### 2.1. Deep Unfolding HSI Reconstruction

Model-based methods [1, 12, 18, 22, 35, 36, 41, 44, 49] usually solve HSI reconstruction in a Bayesian perspective, which is formulated into a MAP optimization problem. HQS [13], ADMM [4], and PGD [2] are common optimization algorithms. These methods usually decouple the data fidelity term and the regularization term of the objective function, resulting in an iterative scheme consisting of alternately solving a data subproblem and a prior subproblem.

The main idea of deep unfolding methods is that model-based iterative optimization algorithms can be implemented equivalently by a stack of recurrent DNN blocks. Such design was originally applied in deep plug-and-play(PNP) methods [25, 32, 45, 47, 48], which utilize a trained denoiser to implicitly express the prior subproblem as a denoising problem. Inspired by PNP, deep unfolding methods are trained end-to-end by jointly optimizing trainable denoisers for specific tasks. GAP-net [26] unfolds the generalized alternating projection (GAP) algorithm and employs trained auto-encoder-based denoisers. DGSM [16] proposes an unfolding model estimation framework using the learned Gaussian Scale Mixture (GSM) prior. These methods typically use the sensing matrix as the degradation matrix or use a neural network to learn the degradation matrix in the data subproblem.

### 2.2. Methods for Exploiting Spectral and Spatial Priors

Model-based methods adopt handcrafted priors to regularize the reconstruction process. The total variation prior is introduced to solve the HSI reconstruction problem [44]. Based on the assumption that HSIs have sparse representations, sparse-based methods [18, 21, 36], exploit the  $\ell_1$  sparsity to regularize the solution. Considering that the pixels of HSIs have strong long-range dependence, non-local based methods [22, 41, 49] have also been proposed.

End-to-end neural networks have been used to exploit data-driven priors [37, 38]. CNNs-based methods exhibit powerful local similarity modeling capabilities.  $\lambda$ -net [28] reconstructs the HSIs through a two-stage procedure. In [27], TSA-Net is proposed to exploit spatial-spectral correlation. Nonetheless, CNN-based methods have limitations in capturing non-local similarities due to their induced biases. Transformer-based methods [6, 20] have been proposed to model the long range dependency of HSIs. MST [6] proposes the S-MSA, which computes cross-covariance across spectrals to generate an attention map encoding the global context implicitly. However, S-MSA models dependency on spectral dimension may sacrifice some useful spatial information of textures and structures, which is important for reproducing high quality HSI images.

### 3. Method

#### 3.1. Problem Formulation

The main components of the CASSI system that contribute to the degradation process include the physical mask, the dispersive prism and the 2D imaging sensor. The mask  $M \in \mathbb{R}^{H \times W}$  is used to modulate HSI signals  $X \in \mathbb{R}^{H \times W \times N_\lambda}$ . The  $n_\lambda^{th}$  wavelength of the modulated image can thus be represented as:

$$X'_{n_\lambda} = M \odot X_{n_\lambda} \quad (1)$$

where  $\odot$  represents the element-wise product. Then the modulated HSI  $X'$  are shifted in the dispersion process, which can be written as:

$$X''(h, w, n_\lambda) = X'(h, w + d_{n_\lambda}, n_\lambda) \quad (2)$$

where  $d_{n_\lambda}$  represents the shifted distance of the  $n_\lambda^{th}$  wavelength. At last, the 2D imaging sensor captures the shifted image into a 2D measurement. This process can be formulated as follow:

$$Y = \sum_{n_\lambda=1}^{N_\lambda} X''_{n_\lambda} \quad (3)$$

where  $Y \in \mathbb{R}^{H \times (W + d_{N_\lambda})}$  denotes the 2D measurement. As such, considering the measurement noise, the matrix-vector form of Eq.3 can be formulated as:

$$y = \Phi x + n \quad (4)$$

where  $\Phi$  is the sensing matrix, generally consider it as the shifted mask, and  $n$  represents the additive noise. HSI restoration aims to recover the high-quality image  $x$  from its degraded measurement  $y$ , which is typically an ill-posed problem.

Model-based methods (e.g., [1, 12, 18, 22, 35, 36, 41, 44, 49]) usually formulate HSI reconstruction as a Bayesian problem, solving Eq.(4) under a unified MAP (maximizing a posterior) framework:

$$\hat{x} = \underset{x}{\operatorname{argmax}} \log P(x | y) = \underset{x}{\operatorname{argmax}} \log P(y | x) + \log P(x) \quad (5)$$

where  $\log P(y | x)$  and  $\log P(x)$  represent the data fidelity and the regularization term, respectively. The data fidelity term is usually defined as an  $\ell_2$  norm, expressing Eq.(5) as the following energy function:

$$\hat{x} = \underset{x}{\operatorname{argmin}} \frac{1}{2} \|y - \Phi x\|_2^2 + \lambda J(x) \quad (6)$$

The Proximal Gradient Descent (PGD) algorithm approximately expresses Eq.(6) as an iterative convergence problem through the following iterative function:

$$\hat{x}^k = \underset{x}{\operatorname{argmin}} \frac{1}{2} \|x - (\hat{x}^{k-1} - \rho \Phi^T (\Phi \hat{x}^{k-1} - y))\|_2^2 + \lambda J(x) \quad (7)$$

where  $\hat{x}^k$  refers to the output of the  $k$ -th iteration,  $\rho$  is the step size. Mathematically, the red part of the above function is a gradient descent operation and the blue part can be solved by the proximal operator  $\operatorname{prox}_{\lambda, J}$ . Thus, it leads to a data subproblem and a prior subproblem, i.e., gradient descent (Eq.(8a)) and proximal mapping (Eq.(8b)):

$$v^k = \hat{x}^{k-1} - \rho \Phi^T (\Phi \hat{x}^{k-1} - y) \quad (8a)$$

$$\hat{x}^k = \operatorname{prox}_{\lambda, J}(v^k) \quad (8b)$$

The PGD algorithm iteratively updates  $v^k$  and  $\hat{x}^k$  until convergence. The traditional PGD algorithm mainly suffers from two issues in the CASSI system. Firstly, since the sensing matrix is obtained from the equidistant lasers of different wavelengths on the sensor, it cannot reflect the device errors caused by phase aberration, distortion and alignment of the continuous spectrum. Therefore, there exist a gap between the sensing matrix and the degradation matrix that used in the gradient descent of PGD. Secondly, the hand-crafted priors have to tweak parameters manually, resulting in limited representation abilities in addition to the slow reconstruction speed. To address these issues, we unfold the PGD algorithm by DNNs and integrate residual degradation learning into the gradient descent step.

#### 3.2. Residual Degradation Learning Unfolding Framework

The whole architecture of our proposed RDLUF is presented in Fig.2(a), which is an unfolding framework of the PGD algorithm based on DNNs. Our RDLUF is composed of several repeated stages. Each stage contains a Residual Degradation Learning Gradient Descent (RDLGD) module and a Proximal Mapping (PM) module, corresponding to the gradient descent (Eq.(8a)) and proximal mapping (Eq.(8b)) in an iteration step of the PGD algorithm, respectively. Additionally, there is a stage interaction between two stages for rich features and stable optimization in a SPatial Adaptive Normalization (SPAN) manner.

**Residual Degradation Learning Gradient Descent.** In a snapshot compressive imaging system, since the sensing matrix is obtained from the equidistant lasers of different wavelengths on the sensor, it cannot reflect the device errors caused by phase aberration, distortion and alignment of the continuous spectrum. Therefore, there still exist a gap between the sensing matrix  $\Phi$  and the degradation matrix  $\hat{\Phi}$ . Previous methods proposed learning the degradation matrix using a neural network. However, it is challenging to directly model the degradation process. It is easier to optimize the residual mapping than to optimize the original, unreferenced mapping. Therefore, instead of directly learning the degradation matrix, we propose the RDLGD module to estimate the residual between the sensing matrix  $\Phi$  and the degradation matrix  $\hat{\Phi}$  from the compressed measurement  $y$  and the sensing matrix  $\Phi$ . The RDLGD's

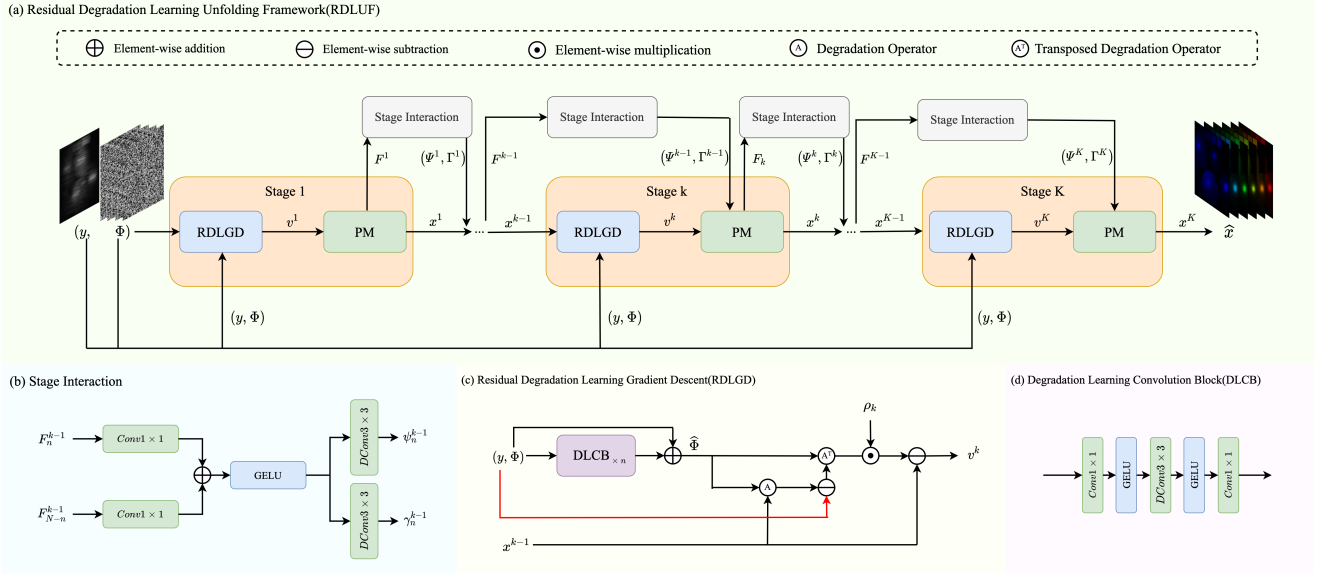


Figure 2. The architecture of our RDLUF with  $K$  stages (iterations). RDLGD and PM denote the Residual Degradation Learning Gradient Descent module and the Proximal Mapping module in each stage. RDLGD estimates the degradation matrix  $\hat{\Phi}$  from the compressed measurement  $y$  and the sensing matrix  $\Phi$  and performs the gradient descent procedure with a learnable parameter step size  $\rho_k$ . There is a stage interaction between stages.

architecture is shown in Fig.2(c), which is consist of several Degradation Learning Convolution Blocks (DLCBs). The DLCB is illustrated in Fig.2(d). The degradation matrix can be calculated as  $\hat{\Phi} = \Phi + \mathcal{R}(y, \Phi)$ , where  $\mathcal{R}$  represents the several cascaded DLCB,  $y$  is the compressed measurement,  $\Phi$  is the sensing matrix.

Thus, without loss of interpretability, the gradient descent in our proposed RDLUF can be defined as the following function:

$$v^k = \hat{x}^{k-1} - \rho^k \hat{\Phi}^{\top k} (\hat{\Phi}^k \hat{x}^{k-1} - y) \quad (9)$$

where  $\rho$  is a learnable parameter,  $k$  represents the number of stage.

**Proximal Mapping.** For the solution of Eq.(8b), it is known that, from a Bayesian perspective, it corresponds to a denoising problem [7, 45]. In this context, we design the Mixing priors across Spectral and Spatial(Mix $S^2$ ) Transformer as the Proximal Mapping(PM) module, shown in Fig.3(a). More details will be illustrated in the next section.

**Stage Interaction.** The proposed stage interaction module normalizes current stage features in a SPatial Adaptive Normalization(SPAN) manner [29, 30]. SPAN uses previous stage features to generate modulation parameters. The calculation of modulation parameters is formulated as eq.(10a, 10b). Then the current stage features are modulated as eq.(10c). The detailed structure is illustrated in Fig.2(b). The proposed stage interaction module has several merits. First, information loss makes the network less vulnerable due to repeated use of up- and down-sampling operations in the encoder-decoder. Second, the multi-scale features of

one stage help enrich the features of the next stage. Third, the network optimization procedure becomes more stable as it eases the flow of information.

$$\psi_n^{k-1} = DCConv(\sigma(Conv(F_n^{k-1}) + Conv(F_{N-n}^{k-1}))) \quad (10a)$$

$$\gamma_n^{k-1} = DCConv(\sigma(Conv(F_n^{k-1}) + Conv(F_{N-n}^{k-1}))) \quad (10b)$$

$$F_n^k = \psi_n^{k-1} \odot \hat{F}_n^k + \gamma_n^{k-1} \quad (10c)$$

where  $\sigma$  represents the activation function,  $F_n^{k-1}$  and  $\hat{F}_n^k$  denote previous stage features and current stage features before normalization of  $n_{th}$  block, respectively.  $\psi_n^{k-1}$ ,  $\gamma_n^{k-1}$  represent the generated modulation parameters of current stage of  $n_{th}$  block respectively.  $k$  is the number of stage and  $N$  is the block number of Mix $S^2$  Transformer.

### 3.3. Mixing priors across Spectral and Spatial Transformer

In this section, we explain the proposed model Mix $S^2$  Transformer in detail.

**Network Architecture.** As shown in Fig.3(a), Mix $S^2$  Transformer adopts a U-shaped structure consists of several basic unit Mix $S^2$  blocks. There are up- and down-sampling modules between Mix $S^2$  blocks. We introduce the block interaction to reduce the loss of information caused by up- and down-sampling operations. Different scale features are interpolated to the same scale in block interaction. Firstly, the Mix $S^2$  Transformer uses a  $conv3 \times 3$  to map  $v_k$  into shallow features  $X_0 \in \mathbb{R}^{H \times \hat{W} \times C}$ , where  $\hat{W} = W + d_{n_x}$ . Secondly,

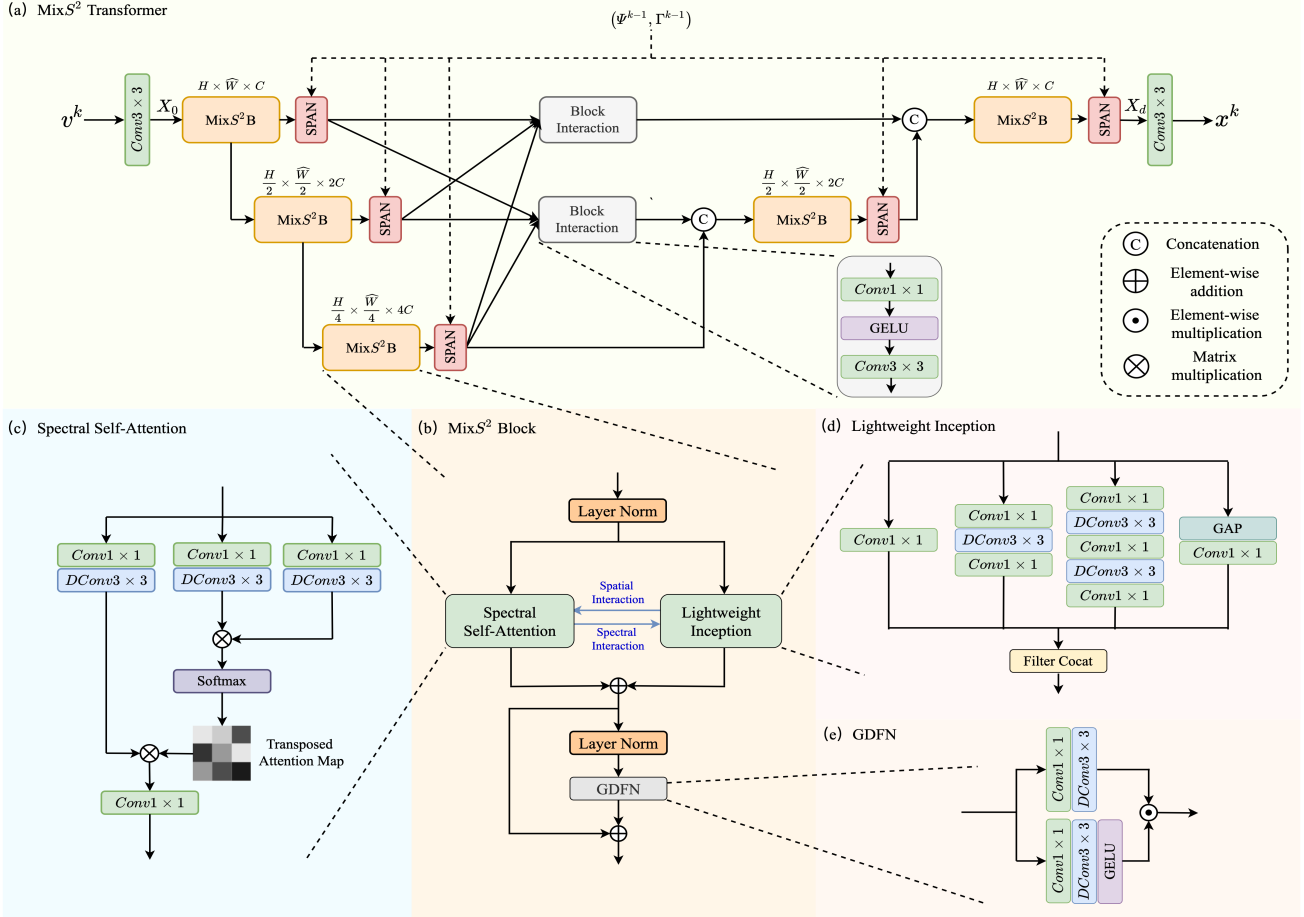


Figure 3. Diagram of the MixS<sup>2</sup> Transformer. (a) MixS<sup>2</sup> Transformer adopts a U-shaped structure with block interactions. (b) The basic unit of the MixS<sup>2</sup> Transformer, MixS<sup>2</sup> block. (c) The structure of the spectral self-attention branch. (d) The structure of the lightweight inception branch. (e) The components of the gated-Dconv feed-forward network (GDFN)

$X_0$  passes through all the MixS<sup>2</sup> blocks and block interactions to be embedded into deep features  $X_d \in \mathbb{R}^{H \times \bar{W} \times C}$ . Finally, a  $\text{conv}3 \times 3$  operates on  $X_d$  to generate the denoised image  $x_k$ .

**Mixing priors across Spectral and Spatial Block.** The most important component of the MixS<sup>2</sup> Transformer is the MixS<sup>2</sup> block as shown in Fig.3(b), which consists of two layer normalization (LN), a spectral self-attention branch, and a lightweight inception branch in a parallel design with a bi-directional interaction and a gated-Dconv Feed-Forward Network (GDFN) [46] that is detailed in Fig.3(e). The up- and down-sampling modules are both a  $\text{conv}3 \times 3$  and a bilinear interpolation with different scale factors. The details of the spectral self-attention branch, lightweight inception branch, and bi-directional interaction are described following.

**Spectral Self-Attention Branch.** The spectral self-attention branch is following [46], which *query*(Q), *key*(K) and *value*(V) are embedded with a  $\text{conv}1 \times 1$  and a  $\text{dconv}3 \times 3$  different from [6]. The key component of

the spectral self-attention branch is the S-MSA. Fig.3(c) shows the spectral self-attention branch. The input  $X_{in} \in \mathbb{R}^{H \times W \times C}$  is first embedded, yielding  $Q = W_d^Q W_p^Q X$ ,  $K = W_d^K W_p^K X$  and  $V = W_d^V W_p^V X$ . Where  $W_p^{(\cdot)}$  is the  $1 \times 1$  point-wise convolution and  $W_d^{(\cdot)}$  is the  $3 \times 3$  depth-wise convolution. Next, S-MSA reshapes the query and key projections such that their dot-product interaction generates a transposed attention map  $A$  of size  $\mathbb{R}^{C \times C}$ . Overall, the S-MSA process is defined as:

$$X = W_p \text{Attention}(Q, K, V) \quad (11)$$

$$\text{Attention}(Q, K, V) = V \text{Softmax}(KQ/\alpha)$$

where  $Q \in \mathbb{R}^{HW \times C}$ ;  $K \in \mathbb{R}^{C \times HW}$ ; and  $V \in \mathbb{R}^{HW \times C}$  matrices are obtained after reshaping tensors from the original size  $\mathbb{R}^{H \times W \times C}$ . Here,  $\alpha$  is a learnable scaling parameter to control the magnitude of the dot product K and Q before applying the softmax function.

**Lightweight Inception Branch.** Corresponding to the multiscale convolution, the structure of the lightweight inception branch follows [33, 34], but the difference is that

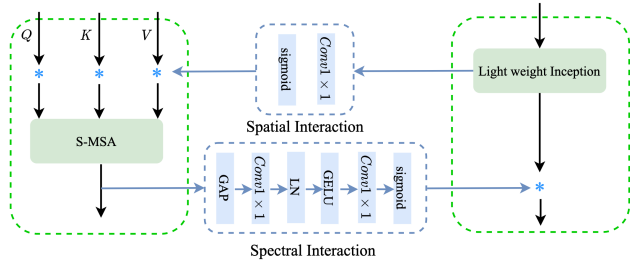


Figure 4. **Detailed design of the bi-directional interaction.** The spatial/spectral interaction provides spatial/spectral context extracted by Spectral Self-Attention/Lightweight Inception to the other path.

we use  $dconv3 \times 3$  instead of  $conv3 \times 3$ , as illustrated in Fig.3(d). The visual information is processed at various scales and then aggregated so that the next layer can abstract features from different scales simultaneously and hence capture more textures and details.

**Bi-directional Interaction.** Familiar with [9], we introduce bi-directional interaction across spectral and spatial branches. For spatial interaction, the output features of the lightweight inception module pass through a  $conv1 \times 1$  with a sigmoid activation to get a spatial attention map, applying to the *query*(Q), *key*(K) and *value*(V) in a spatial attention manner. For spectral interaction, the output features of the spectral self-attention module are fed into a spectral attention module [14] to obtain a spectral attention weight, applied to the output features of the lightweight inception module in a spectral attention manner. More details are shown in Fig.4.

**Block Interaction.** The encoder-decoder networks [5, 8, 19, 31] first gradually map the input to low-resolution representations, and then progressively apply reverse mapping to recover the original resolution. While these models effectively encode multi-scale information, they are prone to sacrificing spatial details due to the repeated use of down-sampling operations. To address this issue, inspired by [10], we introduce the block interaction to allow information flow from different scales within a single  $MixS^2$  Transformer. Each block interaction takes the output of all encoder blocks as an input and combines multiscale features using convolutional layers. The output of the block interaction is delivered to its corresponding decoder block.

## 4. Experiments

### 4.1. Experimental Settings

Following the settings of [6, 16, 27], we adopt 28 wavelengths from 450 nm to 650 nm derived by spectral interpolation manipulation for HSIs. Simulation and real experiments are carried out.

**Simulation HSI Data.** We conduct simulations on two public HSI datasets, CAVE [43] and KAIST [11]. The CAVE dataset is composed of 32 hyperspectral images at a spatial size of  $512 \times 512$ . The KAIST dataset con-

tains 30 HSIs of spatial size  $2704 \times 3376$ . Similar to [6, 15, 16, 20, 27], we employ the real mask of size  $256 \times 256$  and adopt CAVE as the training set. 10 scenes from KAIST are selected for testing.

**Real HSI Data.** We use the real HSI dataset collected by the SD-CASSI system proposed in [27].

**Evaluation Metrics.** The peak signal-to-noise ratio (PSNR) and the structural similarity index (SSIM) [42] are used to evaluate the performance of the HSI reconstruction methods.

**Implementation Details.** The RDLUF-Mix $S^2$  is implemented by PyTorch. All the models are trained with Adam [17] optimizer ( $\beta_1 = 0.9$  and  $\beta_2 = 0.999$ ) using the cosine annealing scheduler [23] for 300 epochs with a linear warm-up. The learning rate is set to  $2 \times 10^{-4}$  and the batch size is set to 1. During training, a patch at the size of  $256 \times 256 \times 28$  and  $660 \times 660 \times 28$  is randomly cropped from the training 3D HSI datasets as labels for the simulation and real experiments. The shift steps  $d$  in dispersion are set to 2. Data augmentations include random flipping and rotation. The models are trained on an RTX 3090 GPU. The training objective is to minimize the Charbonnier loss between the reconstructed and ground-truth HSIs.

### 4.2. Quantitative Results

We compare our RDLUF-Mix $S^2$  with several SOTA HSI reconstruction algorithms, including three model-based methods (TwIST [3], GAP-TV [44], and DeSCI [22]) and four deep learning based methods (DGSMP [16], HDNet [15], MST [6], CST [20]). For fair comparisons, all methods are tested with the same settings as DGSMP [16]. The PSNR and SSIM results of different methods on 10 scenes in the simulation datasets are shown in Tab.1. CNN-based and Transformer-based methods perform better than traditional methods. Our proposed method outperforms CNN-based and Transformer-based methods by a large margin. Compared to DGSMP [16], HDNet [15], MST-L [6] and CST-L\* [20], the proposed method with  $9stage$  achieves improvements over these methods, which are 6.94 dB, 5.23dB, 4.39dB, and 3.45dB on average, respectively. Additionally, our proposed method requires cheaper memory costs as shown in fig.1.

### 4.3. Qualitative Results

**Simulation HSI Reconstruction.** Fig.5 compares the simulation HSI reconstructions of our RDLUF-Mix $S^2$  and seven SOTA algorithms on Scene 5 with 4 out of 28 spectral channels. The restored HSIs retain spatial smoothness at homogeneous regions thanks to the spectral self-attention branch that implicitly model long-range dependence. The introduction of the multiscale convolution branch enhances the ability to model detailed textures, resulting in more detailed content, cleaner textures, and fewer artifacts. Besides, Fig.5 plots the spectral density curves (bottom-left)

Scene	TwIST [3]		GAP-TV [44]		DeSCI [22]		DGSMF [16]		HDNet [15]		MST-L [6]		CST-L* [20]		Ours 3stage		Ours 5stage		Ours 7stage		Ours 9stage	
	PSNR	SSIM	PSNR	SSIM	PSNR	SSIM	PSNR	SSIM	PSNR	SSIM	PSNR	SSIM	PSNR	SSIM	PSNR	SSIM	PSNR	SSIM	PSNR	SSIM	PSNR	SSIM
1	25.16	0.700	26.82	0.754	27.13	0.748	33.26	0.915	34.95	0.948	35.40	0.941	35.96	0.949	36.67	0.953	37.30	0.960	37.65	0.963	<b>37.94</b>	<b>0.966</b>
2	23.02	0.604	22.89	0.610	23.04	0.620	32.09	0.898	32.52	0.953	35.87	0.944	36.84	0.955	38.48	0.965	39.39	0.971	40.45	0.976	<b>40.95</b>	<b>0.977</b>
3	21.40	0.711	26.31	0.802	26.62	0.818	33.06	0.925	34.52	0.957	36.51	0.953	38.16	0.962	40.63	0.971	42.06	0.975	43.00	0.978	<b>43.25</b>	<b>0.979</b>
4	30.19	0.851	30.65	0.852	34.96	0.897	40.54	0.634	43.00	0.981	42.27	0.973	42.44	0.975	46.04	0.986	46.89	0.988	47.40	0.990	<b>47.83</b>	<b>0.990</b>
5	21.41	0.635	23.64	0.703	23.94	0.706	28.86	0.882	32.49	0.957	32.77	0.947	33.25	0.955	34.63	0.963	35.74	0.969	36.78	0.974	<b>37.11</b>	<b>0.976</b>
6	20.95	0.644	21.85	0.663	22.38	0.683	33.08	0.937	35.96	0.965	34.80	0.955	35.72	0.963	36.18	0.966	37.03	0.971	<b>37.56</b>	0.974	37.47	<b>0.975</b>
7	22.20	0.643	23.76	0.688	24.45	0.743	30.74	0.886	29.18	0.937	33.66	0.925	34.86	0.944	35.85	0.951	37.05	0.959	38.25	0.967	<b>38.58</b>	<b>0.969</b>
8	21.82	0.650	21.98	0.655	22.03	0.673	31.55	0.923	34.00	0.961	32.67	0.948	34.34	0.961	34.37	0.963	35.18	0.968	<b>35.86</b>	<b>0.971</b>	35.50	0.970
9	22.42	0.690	22.63	0.682	24.56	0.732	31.66	0.911	34.56	0.957	35.39	0.949	36.51	0.957	38.98	0.966	40.64	0.973	41.71	0.978	<b>41.83</b>	<b>0.978</b>
10	22.67	0.569	23.10	0.584	23.59	0.587	31.44	0.925	32.22	0.950	32.50	0.941	33.09	0.945	33.73	0.950	34.58	0.957	34.83	0.959	<b>35.23</b>	<b>0.962</b>
Avg	23.12	0.669	24.36	0.669	25.27	0.721	32.63	0.917	34.34	0.957	35.18	0.948	36.12	0.957	37.56	0.963	38.59	0.969	39.35	0.973	<b>39.57</b>	<b>0.974</b>

Table 1. The PSNR in dB and SSIM results of the test methods on 10 scenes. RDLUF-Mix $S^2$  Transformer significantly surpass other competitors.

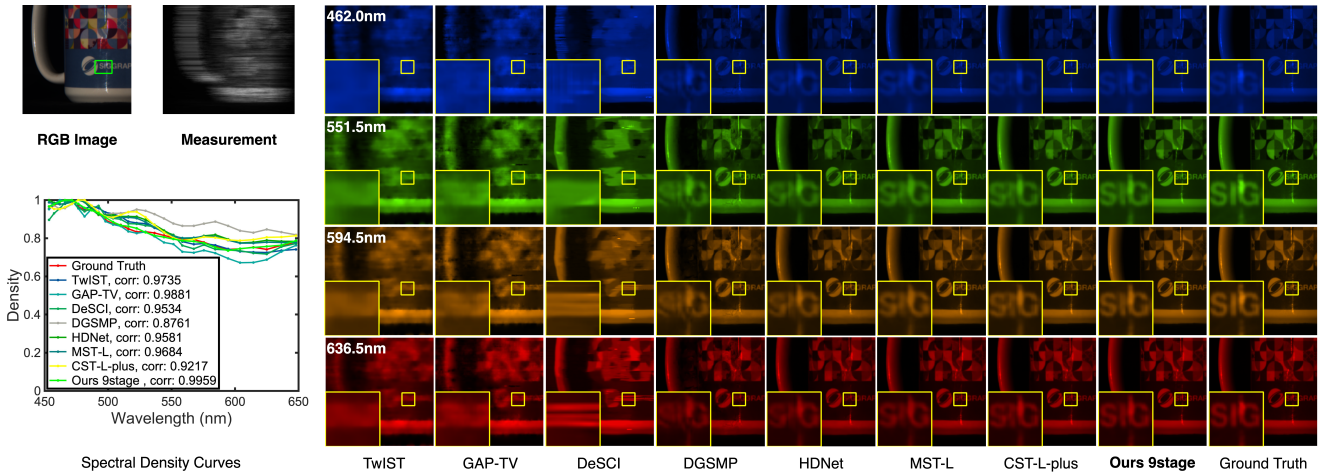


Figure 5. Reconstructed simulation HSI comparisons of Scene 5 with 4 out of 28 spectral channels. 7 SOTA methods and our RDLUF-Mix $S^2$  with 9stage are included. Our method’s results are most clear. A region is selected in the green box for analyzing the spectra of the reconstructed results. Zoom in for a better view.

corresponding to the picked region of the green box in the RGB image (top-left). The highest correlation coefficient between our curve and the ground truth demonstrates the efficacy of spectral consistent reconstruction that benefits from the residual degradation learning strategy that bridges the gap between the sensing matrix and the degradation process.

**Real HSI Reconstruction.** We further apply the proposed method to the real SD-CASSI system [27] that captures real scenes with 28 wavelengths ranging from 450 to 650 nm and has 54-pixel dispersion. Following [6, 16, 20, 27], we retrain our model(RDLUF-Mix $S^2$ ) on CAVE [43] and KAIST [11] datasets. To simulate real measurements, 11-bit shot noise is injected during training. Fig.6 shows reconstructed images of two real scenes (Scene 3 and Scene 4) with 4 of 28 spectral channels between our RDLUF-Mix $S^2$  and seven SOTA methods. In Scene 3, the proposed method is able to restore more texture and detail, especially in the cactus areole area. In Scene 4, the proposed method reconstructs the face in a more natural way. In particular, it restores the clearer right eye than other methods.

#### 4.4. Ablation Study

**Components of Mix $S^2$  structure.** Our goal is to study how each component of Mix $S^2$  structure affects performance, including the Spectral branch(corresponding to the spectral self-attention branch), Spatial branch(corresponding to the lightweight inception branch), Spectral Interaction, and Spatial Interaction. As shown in Tab.2, the method only with the Spectral branch achieves 37.17 dB. When both the Spectral branch and Spatial branch are applied, the method achieves 0.24 dB improvements. The Spectral Interaction and Spatial Interaction respectively achieve 0.07dB and 0.08dB improvements with few parameters. When we exploit all the components jointly, the method gains by 0.39dB. These results demonstrate the effectiveness of Mix $S^2$  structure.

**Residual Degradation Learning.** We conduct ablation studies to verify the impacts of the residual degradation learning of the proposed framework. In the experiment, we remove the residual degradation learning strategy from our RDLUF-Mix $S^2$ , resulting in a plain gradient descent module. As shown in Tab.3, with the residual degradation learning strategy, our RDLUF-Mix $S^2$  Transformer 3stage

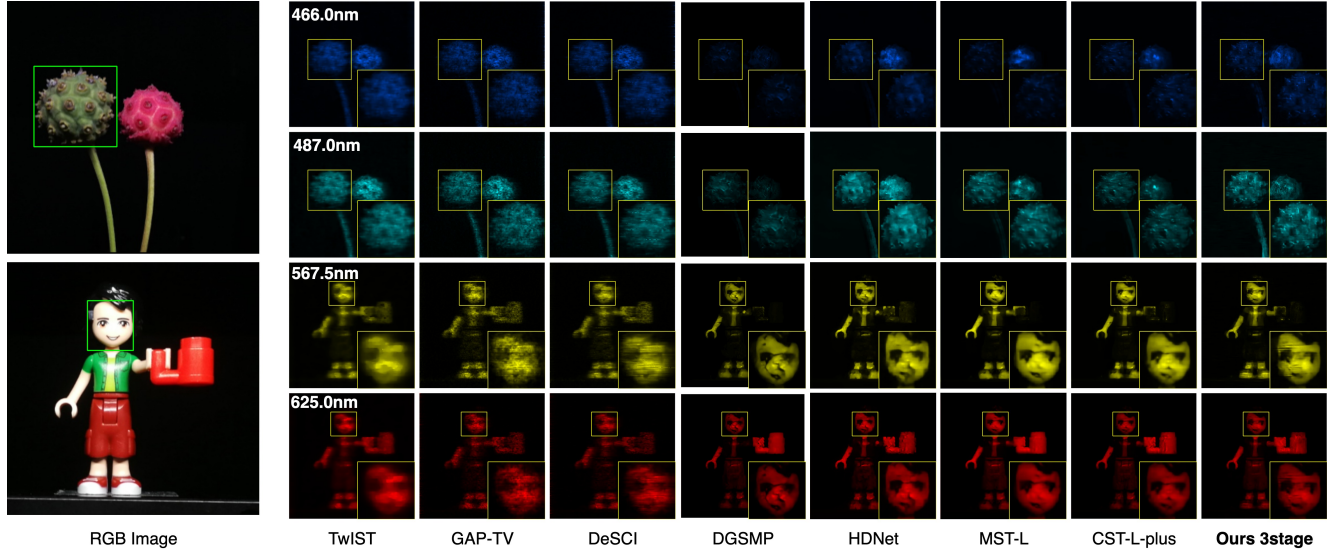


Figure 6. Real HSI reconstruction comparison of Scene 3 and Scene 4. 4 out of 28 spectra are randomly selected.

yields a significant improvement of 0.69dB. This superiority is mainly derived from RDLGD’s ability to learn the gap between the sensing matrix and the degradation process.

**Block Interaction and Stage Interaction.** We conduct ablation studies to investigate the effect of the Block Interaction and the Stage Interaction. To demonstrate the effectiveness of Block Interaction and Stage Interaction, we remove them from our RDLUF-Mix $S^2$  separately. The results are shown in Tab.4. The improvements are mainly because the Stage Interaction and the Block Interaction both reduced the information loss caused by the up- and down-sample operator.

**Number of stages.** Our model shares parameters except for the first and last stages. We explore the gains brought by the number of stages, including 3, 5, 7, and 9 stages. From Tab.5, we can find that the performance increases with the number of stages, demonstrating the effectiveness of the iterative network design. 7stage is the best trade-off between the reconstruction performance and the computational complexity. Interestingly, we observed that sharing parameters can achieve better performance. It may suggest that a well-trained RDLGD module boosts more than multiple different RDLGD modules.

Spectral Branch	Spatial Branch	Spectral Interaction	Spatial Interaction	PSNR	SSIM
✓				37.17	0.961
✓	✓			37.41	0.962
✓	✓	✓		37.48	0.962
✓	✓		✓	37.49	0.962
✓	✓	✓	✓	<b>37.56</b>	<b>0.963</b>

Table 2. Break-down ablation studies for Mix $S^2$  structure.

Residual Degradation Learning	PSNR	SSIM
w/o	36.87	0.958
w	<b>37.56</b>	<b>0.963</b>

Table 3. Ablation of RDLGD module.

Stage Interaction	Block Interaction	PSNR	SSIM
		37.41	0.957
✓		37.49	0.960
	✓	37.50	0.961
✓	✓	<b>37.56</b>	<b>0.963</b>

Table 4. Ablation to study the effect of Stage Interaction and Block Interaction.

Number of stages	PSNR	SSIM
3	37.56	0.963
5	38.59	0.969
7	39.35	0.973
9	<b>39.57</b>	<b>0.974</b>
9*	39.03	0.971

Table 5. Ablation of number of stages. \* notes all parameters is independent.

## 5. Conclusion and Limitation

In this paper, we firstly propose the RDLUF, which bridges the gap between the sensing matrix and the degradation process. Then, to strengthen the spectral-spatial representation capability in HSI, a Mix $S^2$  Transformer is designed via mixing priors across spectral and spatial. Finally, plugging the Mix $S^2$  Transformer into the RDLUF leads to an end-to-end trainable and interpretable neural network RDLUF-Mix $S^2$ . Extensive experimental results on both simulation and real datasets demonstrate that the proposed method outperforms existing state-of-the-art algorithms.

With the introduction of the convolution branch, more computational complexity is also included. Therefore, in the future, we will exploit some efficient implementations to extend our method.

## References

- [1] Gonzalo R Arce, David J Brady, Lawrence Carin, Henry Arguello, and David S Kittle. Compressive coded aperture spectral imaging: An introduction. *IEEE Signal Processing Magazine*, 31(1):105–115, 2013. 1, 2, 3
- [2] Amir Beck and Marc Teboulle. A fast iterative shrinkage-thresholding algorithm for linear inverse problems. *SIAM journal on imaging sciences*, 2(1):183–202, 2009. 2
- [3] José M Bioucas-Dias and Mário AT Figueiredo. A new twist: Two-step iterative shrinkage/thresholding algorithms for image restoration. *IEEE Transactions on Image processing*, 16(12):2992–3004, 2007. 6, 7
- [4] Stephen Boyd, Neal Parikh, Eric Chu, Borja Peleato, Jonathan Eckstein, et al. Distributed optimization and statistical learning via the alternating direction method of multipliers. *Foundations and Trends® in Machine learning*, 3(1):1–122, 2011. 2
- [5] Tim Brooks, Ben Mildenhall, Tianfan Xue, Jiawen Chen, Dillon Sharlet, and Jonathan T Barron. Unprocessing images for learned raw denoising. In *Proceedings of the IEEE/CVF Conference on Computer Vision and Pattern Recognition*, pages 11036–11045, 2019. 6
- [6] Yuanhao Cai, Jing Lin, Xiaowan Hu, Haoqian Wang, Xin Yuan, Yulun Zhang, Radu Timofte, and Luc Van Gool. Mask-guided spectral-wise transformer for efficient hyperspectral image reconstruction. In *Proceedings of the IEEE/CVF Conference on Computer Vision and Pattern Recognition*, pages 17502–17511, 2022. 1, 2, 5, 6, 7
- [7] Stanley H Chan, Xiran Wang, and Omar A Elgendy. Plug-and-play admm for image restoration: Fixed-point convergence and applications. *IEEE Transactions on Computational Imaging*, 3(1):84–98, 2016. 4
- [8] Chen Chen, Qifeng Chen, Jia Xu, and Vladlen Koltun. Learning to see in the dark. In *Proceedings of the IEEE conference on computer vision and pattern recognition*, pages 3291–3300, 2018. 6
- [9] Qiang Chen, Qiman Wu, Jian Wang, Qinghao Hu, Tao Hu, Errui Ding, Jian Cheng, and Jingdong Wang. Mixformer: Mixing features across windows and dimensions. In *Proceedings of the IEEE/CVF Conference on Computer Vision and Pattern Recognition*, pages 5249–5259, 2022. 6
- [10] Sung-Jin Cho, Seo-Won Ji, Jun-Pyo Hong, Seung-Won Jung, and Sung-Jea Ko. Rethinking coarse-to-fine approach in single image deblurring. In *Proceedings of the IEEE/CVF international conference on computer vision*, pages 4641–4650, 2021. 6
- [11] Inchang Choi, MH Kim, D Gutierrez, DS Jeon, and G Nam. High-quality hyperspectral reconstruction using a spectral prior. Technical report, 2017. 6, 7
- [12] MA Figureido, RD Norwak, and SJ Wright. Gradient projection for sparse reconstruction: Application to compressed sensing and other inverse problem. *IEEE J. Sel. Top. Signal Process*, 1(4):586–597, 2007. 2, 3
- [13] Ran He, Wei-Shi Zheng, Tieniu Tan, and Zhenan Sun. Half-quadratic-based iterative minimization for robust sparse representation. *IEEE transactions on pattern analysis and machine intelligence*, 36(2):261–275, 2013. 2
- [14] Jie Hu, Li Shen, and Gang Sun. Squeeze-and-excitation networks. In *Proceedings of the IEEE conference on computer vision and pattern recognition*, pages 7132–7141, 2018. 6
- [15] Xiaowan Hu, Yuanhao Cai, Jing Lin, Haoqian Wang, Xin Yuan, Yulun Zhang, Radu Timofte, and Luc Van Gool. Hd-net: High-resolution dual-domain learning for spectral compressive imaging. In *Proceedings of the IEEE/CVF Conference on Computer Vision and Pattern Recognition*, pages 17542–17551, 2022. 1, 6, 7
- [16] Tao Huang, Weisheng Dong, Xin Yuan, Jinjian Wu, and Guangming Shi. Deep gaussian scale mixture prior for spectral compressive imaging. In *Proceedings of the IEEE/CVF Conference on Computer Vision and Pattern Recognition*, pages 16216–16225, 2021. 1, 2, 6, 7
- [17] Diederik P Kingma and Jimmy Ba. Adam: A method for stochastic optimization. *arXiv preprint arXiv:1412.6980*, 2014. 6
- [18] David Kittle, Kerkil Choi, Ashwin Wagadarikar, and David J Brady. Multiframe image estimation for coded aperture snapshot spectral imagers. *Applied optics*, 49(36):6824–6833, 2010. 1, 2, 3
- [19] Orest Kupyn, Tetiana Martyniuk, Junru Wu, and Zhangyang Wang. Deblurgan-v2: Deblurring (orders-of-magnitude) faster and better. In *Proceedings of the IEEE/CVF International Conference on Computer Vision*, pages 8878–8887, 2019. 6
- [20] Jing Lin, Yuanhao Cai, Xiaowan Hu, Haoqian Wang, Xin Yuan, Yulun Zhang, Radu Timofte, and Luc Van Gool. Coarse-to-fine sparse transformer for hyperspectral image reconstruction. *arXiv preprint arXiv:2203.04845*, 2022. 1, 2, 6, 7
- [21] Xing Lin, Yebin Liu, Jiamin Wu, and Qionghai Dai. Spatial-spectral encoded compressive hyperspectral imaging. *ACM Transactions on Graphics (TOG)*, 33(6):1–11, 2014. 1, 2
- [22] Yang Liu, Xin Yuan, Jinli Suo, David J Brady, and Qionghai Dai. Rank minimization for snapshot compressive imaging. *IEEE transactions on pattern analysis and machine intelligence*, 41(12):2990–3006, 2018. 1, 2, 3, 6, 7
- [23] Ilya Loshchilov and Frank Hutter. Sgdr: Stochastic gradient descent with warm restarts. *arXiv preprint arXiv:1608.03983*, 2016. 6
- [24] Jiawei Ma, Xiao-Yang Liu, Zheng Shou, and Xin Yuan. Deep tensor admm-net for snapshot compressive imaging. In *Proceedings of the IEEE/CVF International Conference on Computer Vision*, pages 10223–10232, 2019. 1
- [25] Tim Meinhardt, Michael Moller, Caner Hazirbas, and Daniel Cremers. Learning proximal operators: Using denoising networks for regularizing inverse imaging problems. In *Proceedings of the IEEE International Conference on Computer Vision*, pages 1781–1790, 2017. 2
- [26] Ziyi Meng, Shirin Jalali, and Xin Yuan. Gap-net for snapshot compressive imaging. *arXiv preprint arXiv:2012.08364*, 2020. 1, 2
- [27] Ziyi Meng, Jiawei Ma, and Xin Yuan. End-to-end low cost compressive spectral imaging with spatial-spectral self-attention. In *European Conference on Computer Vision*, pages 187–204. Springer, 2020. 1, 2, 6, 7

- [28] Xin Miao, Xin Yuan, Yunchen Pu, and Vassilis Athitsos. 1-net: Reconstruct hyperspectral images from a snapshot measurement. In *Proceedings of the IEEE/CVF International Conference on Computer Vision*, pages 4059–4069, 2019. 1, 2
- [29] Chong Mou, Qian Wang, and Jian Zhang. Deep generalized unfolding networks for image restoration. In *Proceedings of the IEEE/CVF Conference on Computer Vision and Pattern Recognition*, pages 17399–17410, 2022. 1, 4
- [30] Taesung Park, Ming-Yu Liu, Ting-Chun Wang, and Jun-Yan Zhu. Semantic image synthesis with spatially-adaptive normalization. In *Proceedings of the IEEE/CVF conference on computer vision and pattern recognition*, pages 2337–2346, 2019. 4
- [31] Olaf Ronneberger, Philipp Fischer, and Thomas Brox. U-net: Convolutional networks for biomedical image segmentation. In *International Conference on Medical image computing and computer-assisted intervention*, pages 234–241. Springer, 2015. 6
- [32] Ernest Ryu, Jialin Liu, Sicheng Wang, Xiaohan Chen, Zhangyang Wang, and Wotao Yin. Plug-and-play methods provably converge with properly trained denoisers. In *International Conference on Machine Learning*, pages 5546–5557. PMLR, 2019. 2
- [33] Christian Szegedy, Sergey Ioffe, Vincent Vanhoucke, and Alexander A Alemi. Inception-v4, inception-resnet and the impact of residual connections on learning. In *Thirty-first AAAI conference on artificial intelligence*, 2017. 5
- [34] Christian Szegedy, Vincent Vanhoucke, Sergey Ioffe, Jon Shlens, and Zbigniew Wojna. Rethinking the inception architecture for computer vision. In *Proceedings of the IEEE conference on computer vision and pattern recognition*, pages 2818–2826, 2016. 5
- [35] Jin Tan, Yanting Ma, Hoover Rueda, Dror Baron, and Gonzalo R Arce. Compressive hyperspectral imaging via approximate message passing. *IEEE Journal of Selected Topics in Signal Processing*, 10(2):389–401, 2015. 2, 3
- [36] Ashwin Wagadarikar, Renu John, Rebecca Willett, and David Brady. Single disperser design for coded aperture snapshot spectral imaging. *Applied optics*, 47(10):B44–B51, 2008. 1, 2, 3
- [37] Lizhi Wang, Chen Sun, Ying Fu, Min H Kim, and Hua Huang. Hyperspectral image reconstruction using a deep spatial-spectral prior. In *Proceedings of the IEEE/CVF Conference on Computer Vision and Pattern Recognition*, pages 8032–8041, 2019. 1, 2
- [38] Lizhi Wang, Chen Sun, Maoqing Zhang, Ying Fu, and Hua Huang. Dnu: Deep non-local unrolling for computational spectral imaging. In *Proceedings of the IEEE/CVF Conference on Computer Vision and Pattern Recognition*, pages 1661–1671, 2020. 1, 2
- [39] Lizhi Wang, Zhiwei Xiong, Dahua Gao, Guangming Shi, and Feng Wu. Dual-camera design for coded aperture snapshot spectral imaging. *Applied optics*, 54(4):848–858, 2015. 1
- [40] Lizhi Wang, Zhiwei Xiong, Dahua Gao, Guangming Shi, Wenjun Zeng, and Feng Wu. High-speed hyperspectral video acquisition with a dual-camera architecture. In *Proceedings of the IEEE Conference on Computer Vision and Pattern Recognition*, pages 4942–4950, 2015. 1
- [41] Lizhi Wang, Zhiwei Xiong, Guangming Shi, Feng Wu, and Wenjun Zeng. Adaptive nonlocal sparse representation for dual-camera compressive hyperspectral imaging. *IEEE transactions on pattern analysis and machine intelligence*, 39(10):2104–2111, 2016. 1, 2, 3
- [42] Zhou Wang, Alan C Bovik, Hamid R Sheikh, and Eero P Simoncelli. Image quality assessment: from error visibility to structural similarity. *IEEE transactions on image processing*, 13(4):600–612, 2004. 6
- [43] Fumihito Yasuma, Tomoo Mitsunaga, Daisuke Iso, and Shree K Nayar. Generalized assorted pixel camera: post-capture control of resolution, dynamic range, and spectrum. *IEEE transactions on image processing*, 19(9):2241–2253, 2010. 6, 7
- [44] Xin Yuan. Generalized alternating projection based total variation minimization for compressive sensing. In *2016 IEEE International Conference on Image Processing (ICIP)*, pages 2539–2543. IEEE, 2016. 1, 2, 3, 6, 7
- [45] Xin Yuan, Yang Liu, Jinli Suo, and Qionghai Dai. Plug-and-play algorithms for large-scale snapshot compressive imaging. In *Proceedings of the IEEE/CVF Conference on Computer Vision and Pattern Recognition*, pages 1447–1457, 2020. 2, 4
- [46] Syed Waqas Zamir, Aditya Arora, Salman Khan, Munawar Hayat, Fahad Shahbaz Khan, and Ming-Hsuan Yang. Restormer: Efficient transformer for high-resolution image restoration. In *Proceedings of the IEEE/CVF Conference on Computer Vision and Pattern Recognition*, pages 5728–5739, 2022. 5
- [47] Kai Zhang, Wangmeng Zuo, Shuhang Gu, and Lei Zhang. Learning deep cnn denoiser prior for image restoration. In *Proceedings of the IEEE conference on computer vision and pattern recognition*, pages 3929–3938, 2017. 2
- [48] Kai Zhang, Wangmeng Zuo, and Lei Zhang. Deep plug-and-play super-resolution for arbitrary blur kernels. In *Proceedings of the IEEE/CVF Conference on Computer Vision and Pattern Recognition*, pages 1671–1681, 2019. 2
- [49] Shipeng Zhang, Lizhi Wang, Ying Fu, Xiaoming Zhong, and Hua Huang. Computational hyperspectral imaging based on dimension-discriminative low-rank tensor recovery. In *Proceedings of the IEEE/CVF International Conference on Computer Vision*, pages 10183–10192, 2019. 1, 2, 3
- [50] Xuanyu Zhang, Yongbing Zhang, Ruiqin Xiong, Qilin Sun, and Jian Zhang. Herosnet: Hyperspectral explicable reconstruction and optimal sampling deep network for snapshot compressive imaging. In *Proceedings of the IEEE/CVF Conference on Computer Vision and Pattern Recognition*, pages 17532–17541, 2022. 1